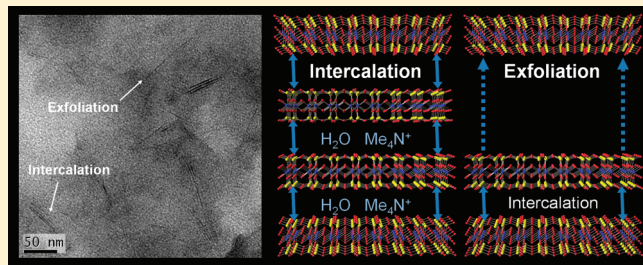


Mechanical Performance and Electrochemical Properties of Clathrate Hydrate Reinforced by Clay Particles

Jong-Ho Cha,^{†,‡} Minchul Kwon,[†] Wonhee Lee, and Huen Lee^{*}

Department of Chemical and Biomolecular Engineering (BK21 program) and Graduate School of EEWS, Korea Advanced Institute of Science and Technology (KAIST), 291 Daehak-ro, Yuseong-gu, Daejeon 305-701, Republic of Korea

ABSTRACT: Clathrate hydrates have increasingly attracted attention as a potential proton conductor because of their relatively high proton conductivity, even at low temperature. For application to various electrochemical energy devices, however, their relatively poor mechanical properties, stemming from the hydrogen bonded frameworks, will have to be improved. At the same time, any accompanying structural transformation that would cause a loss of inherent structural characteristics must be avoided. In the present work, we prepared a clathrate $\text{Me}_4\text{NOH} \cdot 5\text{H}_2\text{O}$ nanocomposite incorporating clay particles to improve its mechanical properties. It was found that clay loading induced an increase in compressive strength from 7.95 MPa for pristine clathrate to 18.25 MPa for 2 wt % clay nanocomposite. This improvement could be attributed to good compatibility between the clathrate hydrate matrix and clay particles and dispersion of the clay into the matrix on a nanometer scale. In addition, we checked the proton conductivity and potential window of the nanocomposite to confirm that they are sufficient for real applications, even at low temperature.



INTRODUCTION

Nanocomposites are defined as two- or multiphase solid materials, where one of the phases is dispersed throughout the bulk phase at a nanosized dimension.¹ In general, solid combination of a bulk matrix and nanodimensional phase (usually <5 wt %) differing in physical and structural properties can result in enhancement of the physicochemical properties of the matrix, that is, mechanical,² electrical,³ optical,⁴ thermal,⁵ and catalytic properties.⁶ For this reason, nanocomposites have drawn substantial interest for both industrial applications and academic research fields instead of conventional composite materials. It is believed that large interfacial area between nanofillers and the matrix materials, good mutual compatibility, and good dispersion of fillers on a nanosized scale are important factors with respect to improving the properties of nanocomposites. With this understanding, researchers have attempted to incorporate various types of inorganic and organic additives, that is, clays, ceramics, carbon nanotubes, and organic fibers, with polymer, ceramic, carbon form, and aerogel matrixes to produce high-performance nanocomposites.^{1,7–11} Notably, layered silicate clays have been the most widely studied additives for enhancing the physical properties of matrixes because they are both inexpensive and environmentally friendly. Furthermore, their high aspect ratio, high surface area, and controllable hydrophilicity through an ion exchange reaction of inorganic cations with organic cations in their interlayers allow various types of media to be mechanically reinforced, even at lower concentrations of clay particles.⁷

Peralkylammonium salts are known to form clathrate structures, where simple hydrophilic anions of halides or hydroxides build host frameworks via hydrogen bonding with water molecules,

whereas large sized cations are enclathrated in the cages of the framework in hydrophobic manner.¹² The size and the shape of the cations as well as the types of anionic species therefore determine the clathrate-formation capability of guest molecules and influence structural transformation with variation of the hydration number as well as the crystal structure of clathrate.¹³ One of the notable features of these ionic clathrates is that protons of water frameworks tend to be more mobile than those of nonionic hydrates, owing to the incorporation of anions in the framework.¹⁴ Clathrates have been accordingly explored as a potential proton conductor over the last few decades.^{15,16}

Among the various types of ionic clathrate hydrates, $\text{Me}_4\text{NOH} \cdot 5\text{H}_2\text{O}$ has increasingly attracted interest as a potential proton conductor owing to both relatively high conductivity and high melting temperature.¹⁶ On the basis of these desirable characteristics, $\text{Me}_4\text{NOH} \cdot 5\text{H}_2\text{O}$ was reported to be able to serve as a proton conductor in an actual nickel–metal battery system.^{16b} More recently, we successfully detected the existence of H_2 gas using an electrochemical H_2 detection sensor assembled with $\text{Me}_4\text{NOH} \cdot 5\text{H}_2\text{O}$, even at low concentrations of H_2 and a low temperature of -20°C .¹⁷ Despite these good performances arising from high conductivity and good compatibility with electrode materials, relatively poor mechanical properties of $\text{Me}_4\text{NOH} \cdot 5\text{H}_2\text{O}$ limit its applicability and also lead to difficulties in preparing electrochemical devices where complicated elements are combined with the conductor.^{16d} Furthermore, loading by

Received: February 17, 2011

Revised: June 28, 2011

Published: July 07, 2011

stacking of some elements and possible external impact or forces could place severe mechanical stress on the conductor during operation, leading to the development of cracking or fracture of the conductor. Accordingly, efforts have been made to increase considerably its mechanical properties by manipulating microstructures of the clathrate hydrates. To this end, we synthesized a $\text{Me}_4\text{NOH} \cdot 5\text{H}_2\text{O}$ clathrate nanocomposite incorporating clay particles that serve as a reinforcement phase. For nanoscale dispersion into the hydrate phase, hydrophilic sodium montmorillonite (Na-MMT), which consists of regular stacks of aluminosilicate layers and sodium cations occupying the interlayer space, has been employed. Consequently, we successfully produced a nanocomposite possessing enhanced compressive strength by good dispersion of intercalated and exfoliated clay particles into the $\text{Me}_4\text{NOH} \cdot 5\text{H}_2\text{O}$ phase. In addition, we evaluated the electrochemical properties, including proton conductivity and potential window, to confirm that the nanocomposite can still be adopted in electrochemical devices, particularly at low temperature, where pristine $\text{Me}_4\text{NOH} \cdot 5\text{H}_2\text{O}$ can be applied. The aim of the present work, therefore, is to prepare a clathrate hydrate nanocomposite that exhibits excellent mechanical and electrochemical performances and potentially can be used in solid proton conductors of various types of electrochemical energy devices.

■ EXPERIMENTAL METHODS

$\text{Me}_4\text{NOH} \cdot 5\text{H}_2\text{O}$ (a purity of 97%) and Na-MMT (SWy-2, collected from Crook County, WY) were acquired from Aldrich and the Source Clays Repository of the Clay Minerals Society at Purdue University, West Lafayette, IN, respectively, and used as received. Na-MMT/ $\text{Me}_4\text{NOH} \cdot 5\text{H}_2\text{O}$ nanocomposite was prepared as follows. We mixed and dispersed 1, 2, 3, and 4 wt % of Na-MMT, respectively, with liquid $\text{Me}_4\text{NOH} \cdot 5\text{H}_2\text{O}$ by alternating between sonication (40 kHz, 150 W) and magnetic stirring at 74 °C. The dispersion process was continued until no aggregated clay particles were observed on the bottom of the bottle by the naked eye. Then, the mixture was cooled to room temperature for the crystallization.

The compressive properties of the nanocomposite were measured using an Instron 4206 compressive test system (Instron Series IX Automated Materials Tester, version 8.28.00). For the preparation of compressive specimens, liquid dispersions were poured in a Teflon mold with an inner diameter of 1.0 cm and a height of 4.0 cm and were crystallized at room temperature. Solidified specimens were removed from the mold and cut to dimensions with 18.5 ± 1.0 mm height. The compressive test was carried out at -20 °C under relative humidity of 50%. The crosshead speed was set at 0.5 mm/min with a preload of 0.1 kN, and more than six specimens were used for each measurement. The obtained load-displacement data were converted to stress-strain data. The results of the two specimens showing the maximum and minimum value were discarded. For the transmission electron microscope (TEM) analysis, an ultrathin section of 90 nm was cut using a diamond knife with a Leica EM UC7/FC7 cryo-ultramicrotome cooled with liquid N₂ at -120 °C. The specimen was placed onto a carbon-coated grid, dried, and then examined under a Technai G2 Spirit Twin TEM fitted with an anti-contaminator (FEI, OR) operated at 120 KV. Images were recorded on a 1K × 1K CCD, multiscan camera model 794 (Gatan, CA) with a resolution of 3.4 Å. The gallery width of the Na-MMT in the nanocomposite was characterized by powder X-ray diffraction (PXRD). The specimens were ground to a fine

powder (~ 200 μm) and recorded on a Rigaku D/MAX-2500 with a light source of graphite-monochromatized Cu Kα1 radiation with a wavelength of 1.5406 Å at a generator voltage of 40 kV and a current of 300 mA. The PXRD experiment was carried out in step mode with a fixed time of 2 s and a step size of 0.03° for $2\theta = 3 - 10^\circ$ at -20 °C. The ionic conductivities were obtained by a complex impedance analysis using a Solartron 1260 impedance/gain-phase analyzer and a 1287 electrochemical interface. This apparatus was connected to a Teflon-coated cell containing a pair of SUS electrodes (1.1 cm × 0.6 cm), situated 4.5 mm apart. The liquid-state nanocomposite was placed between the two electrodes and crystallized at room temperature for the measurement. The real and imaginary parts of the complex impedance were plotted over a frequency range from 10 to 10^6 Hz. The ionic conductivities were calculated from the bulk resistance (R_b), which was identified in a complex impedance diagram using the equation $\sigma = L/R_bA$, where L (4.5 mm) and A (4.0 mm × 4.5 mm) are the distance between the two electrodes and the cross-sectional area of the specimen, respectively. The cyclic voltammetry (CV) was also measured by a Solartron 1260 impedance/gain-phase analyzer and a 1287 electrochemical interface. A glassy carbon electrode was used with a platinum counter and silver reference electrodes. The scan rate was 5 mV·s⁻¹. The differential scanning calorimetry (DSC) thermogram was determined in a sealed aluminum pan at cooling and heating rates of 10 °C·min⁻¹ under a N₂ atmosphere using a NETZSCH DSC 204 F1.

■ RESULTS AND DISCUSSION

Representative compressive stress versus strain curves and average values of compressive strength for pristine $\text{Me}_4\text{NOH} \cdot 5\text{H}_2\text{O}$ and clay/ $\text{Me}_4\text{NOH} \cdot 5\text{H}_2\text{O}$ nanocomposites are given in Figure 1. Each composite, containing 1, 2, 3, and 4 wt % of Na-MMT, respectively, exhibits an initial linear region corresponding to elastic deformation and a permanent plastic deformation region beyond its elastic limit (Figure 1a). In this curve, the compressive strength is assigned as the highest value of stress. Neat $\text{Me}_4\text{NOH} \cdot 5\text{H}_2\text{O}$ shows a compressive strength and compressive modulus of 7.33 and 1248 MPa, respectively, with brittleness. However, the load of clay in the hydrate matrix substantially increases the corresponding compressive strength, finally reaching a highest value of 18.24 MPa for the 2 wt % clay composite. At the same time, the strain value where the maximum stress is manifested, defined as the maximum strain, considerably increases. Above 2 wt % of clay, the compressive strength again slightly decreases with the appearance of relative ductility as more clay particles are incorporated into the hydrate matrix. The relationship between the clay loading and average compressive strength for more than four measurements is described in Figure 1b, which clearly shows the compressive strength increased to 130% (from 7.95 to 18.25 MPa) relative to the pristine hydrate. In this diagram, considerable scattering of the compressive strength is shown for each composite. This might be attributable to the sensitivity of the hydrogen-bonded water frameworks of the nanocomposite to any imperfections of the bulk specimen caused by possible air bubbles, voids, and cracks, similar to ice.¹⁸ Meanwhile, it is observed that the modulus values calculated from the slope of the linear region of strain-stress curves generally did not increase, even though the compressive strength increased substantially (Table 1). However, a higher modulus, when compared with pristine $\text{Me}_4\text{NOH} \cdot 5\text{H}_2\text{O}$, can be seen at 2 wt % clay

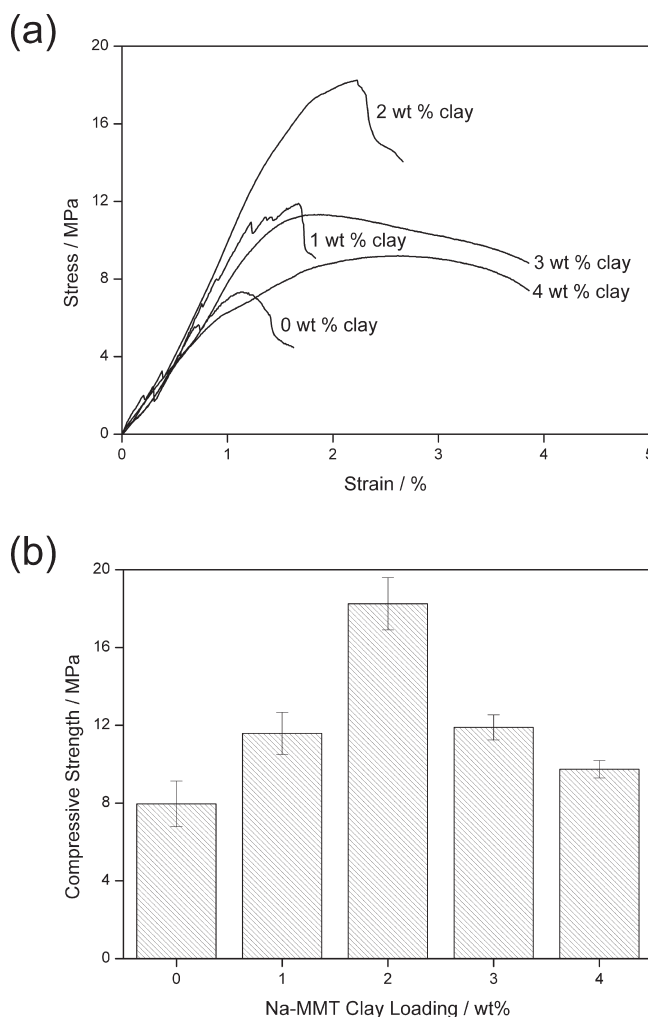


Figure 1. (a) Compressive stress versus strain curves for $\text{Me}_4\text{NOH}\cdot 5\text{H}_2\text{O}$ and clay/ $\text{Me}_4\text{NOH}\cdot 5\text{H}_2\text{O}$ nanocomposite at a crosshead speed of 0.5 mm/min and (b) compressive strength averages for $\text{Me}_4\text{NOH}\cdot 5\text{H}_2\text{O}$ and clay/ $\text{Me}_4\text{NOH}\cdot 5\text{H}_2\text{O}$ nanocomposite with error bars.

loading, where the compressive strength is maximal. The significant increase of both the compressive strength and modulus demonstrates that the clathrate hydrate-based nanocomposite is mechanically reinforced with increasing stiffness, indicating difficulty to deform due to the existence of the clay phase, especially at 2 wt % clay loading. The compressive strength, modulus, and maximum strain are listed in Table 1.

The results for the compressive strength of the nanocomposite indicate that the clay particles play an important role in enhancing the mechanical properties of the clathrate hydrate matrix, very similar to that in the case of clay–polymer nanocomposites.^{7,20} Na-MMT, used in this study, is known to be relatively hydrophilic because of hydrated Na^+ ions occupying the interlayer space in clay particles. Here we conjecture that the compatibility of the clay and hydrate, and the resulting microstructure of clay particles in the hydrate crystalline matrix strongly influence the mechanical performance. Therefore, we examined TEM photographs of the nanocomposite to visualize the internal structure and spatial distribution of the clay particles. At 2 wt % clay loading, both intercalated and exfoliated clay with a high aspect ratio could be observed in the matrix (Figure 2a). Furthermore, individual platelets were well-dispersed through the matrix. It was

Table 1. Mechanical Properties of $\text{Me}_4\text{NOH}\cdot 5\text{H}_2\text{O}$ and clay/ $\text{Me}_4\text{NOH}\cdot 5\text{H}_2\text{O}$ Nanocomposite

compound	Na-MMT (wt %)	compressive strength (MPa)	Young's modulus (10^2 MPa)	max strain (%)
$\text{Me}_4\text{NOH}\cdot 5\text{H}_2\text{O}$		7.95 ± 1.17	8.98 ± 2.44	1.74 ± 0.42
clay/ $\text{Me}_4\text{NOH}\cdot 5\text{H}_2\text{O}$	1	11.58 ± 1.08	7.04 ± 2.36	2.50 ± 0.59
	2	18.25 ± 1.34	14.63 ± 5.20	2.74 ± 0.40
	3	11.89 ± 0.64	8.55 ± 0.99	3.18 ± 1.43
	4	9.74 ± 0.44	10.54 ± 2.18	2.26 ± 0.39

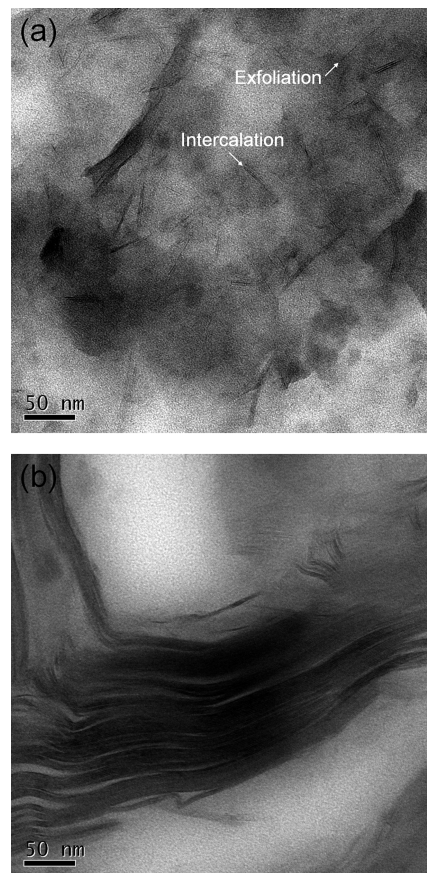


Figure 2. TEM photographs of clay/ $\text{Me}_4\text{NOH}\cdot 5\text{H}_2\text{O}$ nanocomposite with (a) 2 wt % Na-MMT and (b) 4 wt % Na-MMT (scale bar = 50 nm).

found that the clay particles at 4 wt % loading mainly agglomerate together, largely without exfoliated particles, because of the high concentration of clay (Figure 2b). The difference in the particle distributions indicates that the dispersion of particles in the 2 wt % clay nanocomposite is much better than that in the 4 wt % case. We could therefore rationalize that the 2 wt % case, which exhibits the best mechanical properties, possesses significantly increased interfacial area between clay particles and the surrounding hydrate matrix as a result of both intercalated and exfoliated clay particles with good dispersion.

Subsequently, we evaluated the interlayer distance of the silicate layers of Na-MMT in the hydrate matrix using the PXRD technique to confirm the formation of an intercalation structure. Figure 3a shows the diffraction patterns of the nanocomposite at low 2θ ranges of $5\text{--}7^\circ$. The characteristic peaks assigned to the (001) plane reflection of Na-MMT appear at $2\theta = 6.2$ to 6.3° , corresponding to d spacing of 14.16, 14.13, 13.98, and 13.90 Å

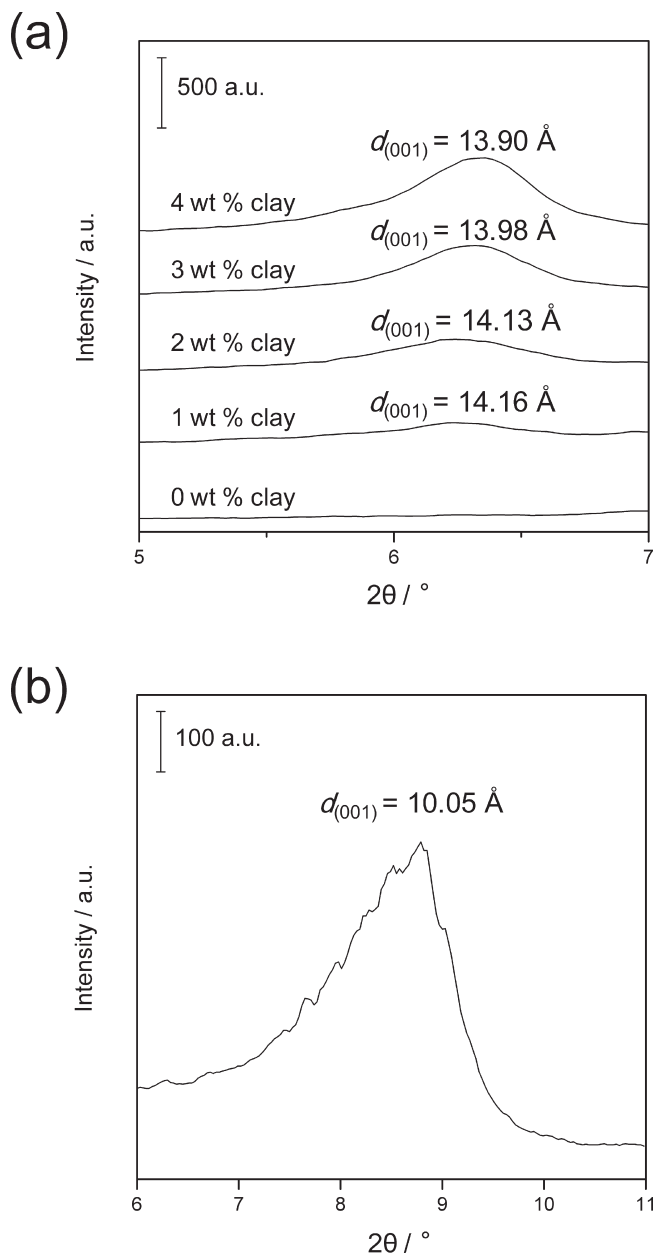


Figure 3. PXRD profiles for the (001) reflection of (a) $\text{Me}_4\text{NOH} \cdot \text{SH}_2\text{O}$ and clay/ $\text{Me}_4\text{NOH} \cdot \text{SH}_2\text{O}$ nanocomposite and (b) pristine Na-MMT.

for 1, 2, 3, and 4 wt % loading of the clay composite, respectively. In comparison with pristine Na-MMT (Figure 3b), an increase in d spacing value indicating the distance between adjacent lattice planes and the resulting decrease in 2θ angle explained by Bragg's law¹⁹ implies an increase in the gallery width due to successful intercalation of the matrix materials into the clay layer structure.²⁰ However, the peak becomes intense and sharp at higher clay loading as more nonexfoliated clay particles are formed. This could, to some extent, be confirmed by a TEM photograph showing agglomerated particles in the 4 wt % clay composite (Figure 2b). At 2 wt % clay loading, where the best compressive strength was obtained, the existence of both intercalated and exfoliated clay particles with good dispersion in the hydrate matrix could be identified through TEM and XRD analyses. In fact, when external loading was applied to the

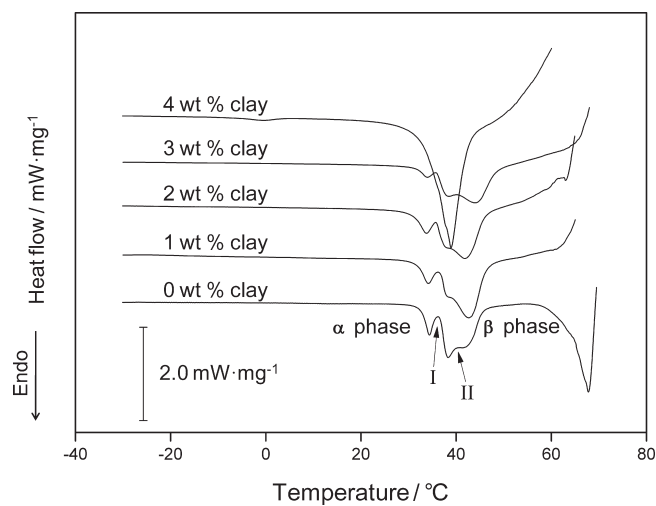


Figure 4. DSC thermograms of $\text{Me}_4\text{NOH} \cdot \text{SH}_2\text{O}$ and clay/ $\text{Me}_4\text{NOH} \cdot \text{SH}_2\text{O}$ nanocomposite at a heating rate of $10 \text{ }^{\circ}\text{C} \cdot \text{min}^{-1}$.

nanocomposite, the stress transfers from the matrix to the nanophase filler via the shear stress at the interface between the filler and matrix, and the filler thereby carries more load than the matrix.¹ Good dispersion of high modulus nanophase with large interfacial area is therefore a significant factor with respect to enhancing the mechanical properties of the matrixes. From this point of view, good dispersion of much stiffer clay particles with high aspect ratio into the clathrate matrix and large contact area tracing from intercalation and exfoliation are believed to provide mechanical reinforcement of the clathrate matrix. We also note that some polymer/clay nanocomposites as well as the clathrate nanocomposite presented in this work have shown similar trends by both intercalation and exfoliation of clay particles.²¹ In most nanocomposites, the mechanical strength was reported to have maximum value at specific concentration of nanophase filler. For the clathrate hydrate nanocomposite, the optimal concentration of clay particles for maximizing compressive resistance would be ~ 2 wt % loading. At this concentration, rigid clay particles with a high aspect ratio and good compatibility with the hydrate could effectively prevent fracture of the matrix and reinforce the nanocomposite against external compressive force. In contrast, a lower concentration of dispersed clay particles does not yield improved mechanical properties. Furthermore, large stress concentration at the interface of large sized aggregations might lead to the development of cracks even at lower compressive stress, and thereby the compressive strength could not be further improved at higher clay concentration.

In addition to mechanical and structural characteristics, it is necessary to investigate the thermal and electrochemical properties for determining the operating conditions of this nanocomposite. Figure 4 exhibits the DSC traces of $\text{Me}_4\text{NOH} \cdot \text{SH}_2\text{O}$ and its nanocomposite. The endothermic peaks confirm that the thermogram of $\text{Me}_4\text{NOH} \cdot \text{SH}_2\text{O}$ consists of multiple solid-solid phase transitions ($\alpha \rightarrow \text{I}$, $\text{I} \rightarrow \text{II}$, and $\text{II} \rightarrow \beta$) and solid-liquid phase transitions near 40 and $68 \text{ }^{\circ}\text{C}$, respectively, which correspond closely to those observed in previous works.^{16c,d} However, the incorporation of even a small amount of clay lead to the disappearance of the melting peak at $68 \text{ }^{\circ}\text{C}$ and consequently lowered the melting temperature to $\sim 43 \text{ }^{\circ}\text{C}$. This tendency is very similar to the results obtained in polymer- $\text{Me}_4\text{NOH} \cdot \text{SH}_2\text{O}$ composites.^{16d} The complex solid-phase

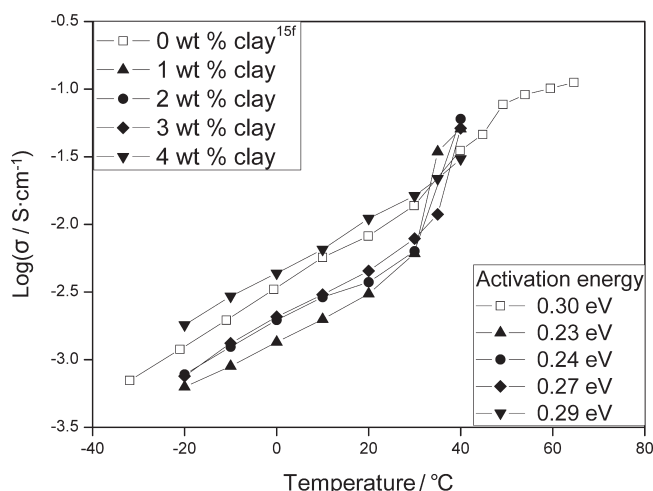


Figure 5. Temperature dependence of ionic conductivities and activation energies for $\text{Me}_4\text{NOH}\cdot\text{SH}_2\text{O}$ and clay/ $\text{Me}_4\text{NOH}\cdot\text{SH}_2\text{O}$ nanocomposite.

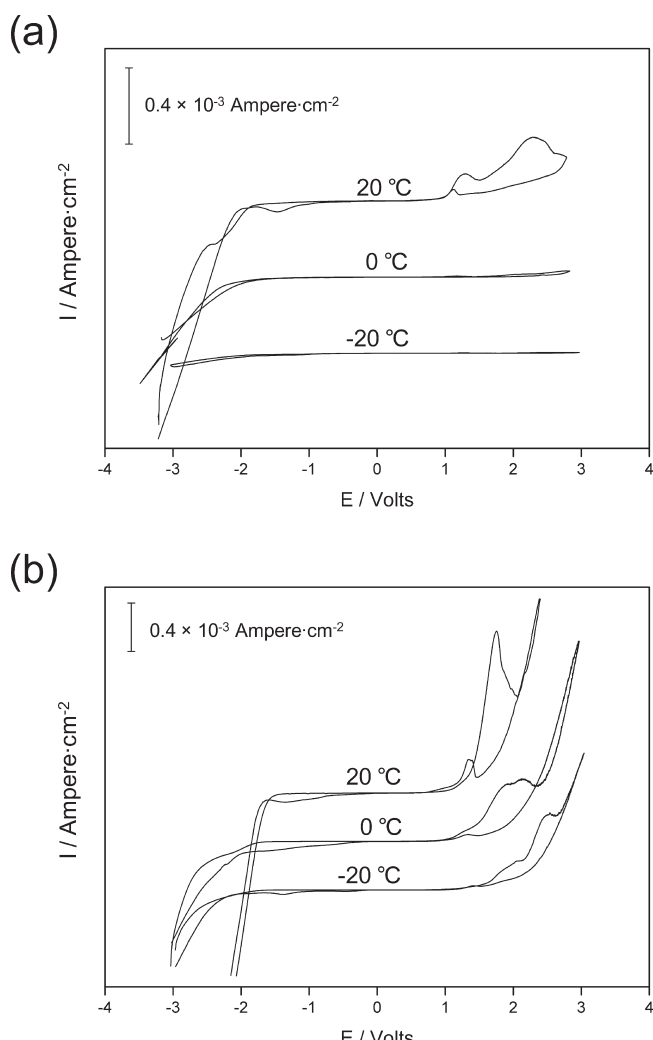


Figure 6. Cyclic voltammograms for (a) $\text{Me}_4\text{NOH}\cdot\text{SH}_2\text{O}$ and (b) clay/ $\text{Me}_4\text{NOH}\cdot\text{SH}_2\text{O}$ nanocomposite with 2 wt % Na-MMT at 20, 0, and -20 °C. The scan rate was 5 mV·s⁻¹.

transition patterns near 40 °C almost remain intact in the thermograms, excluding the 4 wt % clay composite case.

Despite considerable loss of inherent structural characteristics in $\text{Me}_4\text{NOH}\cdot\text{SH}_2\text{O}$, the nanocomposite has a higher melting temperature of ~43 °C, which is sufficient for adoption in solid electrolyte materials compared with that of $\text{Me}_4\text{NOH}\cdot 9\text{H}_2\text{O}\cdot\text{KOH}$ in our previous work.^{15f}

Therefore, we further attempted to determine the ionic conductivities for the clay-hydrate nanocomposite, and the results are shown in Figure 5. The pristine $\text{Me}_4\text{NOH}\cdot\text{SH}_2\text{O}$ exhibits a relatively high conductivity of approximately $10^{-3}\sim 10^{-1} \text{ S}\cdot\text{cm}^{-1}$ in a temperature range of -30~+65 °C accompanying enhanced conductivity near 40 °C, where a solid-phase transition occurs. Similarly, the nanocomposite also shows conductivity values of $10^{-3.3}\sim 10^{-1.3} \text{ S}\cdot\text{cm}^{-1}$ and activation energies (E_a) of ~0.25 eV at -20~+40 °C with conductivity enhancement near 35 °C despite clay incorporation. The findings demonstrate that clay particles do not significantly influence the ionic conduction along hydrogen bonds in the hydrate matrix, which has nearly intact structural characteristics of α, I, and II phases. However, the 4 wt % clay composite exhibits a linear increase in the conductivity without enhancement because of the absence of any solid–solid transitions. Finally, we assessed the electrochemical stability regions for pristine $\text{Me}_4\text{NOH}\cdot\text{SH}_2\text{O}$ and its composite at 20, 0, and -20 °C (Figure 6). The cyclic voltammogram shows that $\text{Me}_4\text{NOH}\cdot\text{SH}_2\text{O}$ is stable in the range of -2.0 ~ +1.0 V versus Ag/Ag^+ at room temperature, indicating a potential window of 3.0 V. A decrease in the temperature enlarges the potential window to 4.0 and 5.0 V at 0 and -20 °C, respectively. This trend is also found for 2 wt % clay loading, where the best compressive strength is exhibited, showing values of 2.7, 3.2, and 3.9 V at 20, 0, and -20 °C, respectively. It should be noted that possessing a large potential window is in high demand for electrochemical devices because out of this range they start to be electrolyzed. To date, there have been few studies on solid electrolytes with high conductivity even at low temperature other than clathrate hydrates.²² Pristine $\text{Me}_4\text{NOH}\cdot\text{SH}_2\text{O}$ and its clay nanocomposite have both relatively high conductivity and a large potential window and meet the requirements of electrolytes used in energy conversion, electrochemical sensing, and reactor systems operating at low temperature.

CONCLUSIONS

In this study, it was shown that adding clay particles to a clathrate matrix can substantially enhance its mechanical performance by exploiting the nature and properties of the clay particles, which are hydrophilic and compatible with the matrix. The resulting compressive strength was shown to increase by 130%, and thereby a maximum value of 18.25 MPa could be achieved when 2 wt % of clay was loaded. This enhancement could be mainly attributed to good dispersion of much stiffer clay particles with a high aspect ratio into the clathrate matrix and the large contact area between the two phases. Through this approach, the poor mechanical properties that constitute a significant drawback of hydrates could be overcome to a significant extent, and a new proton conductor offering enhanced mechanical properties is suggested. In addition, we also obtained excellent electrochemical performance for the nanocomposite, even below 0 °C, indicating that it would be suitable for low-temperature applications. Nevertheless, improved mechanical and physicochemical properties might be still required for real applications. Understanding the physical and structural properties of both the reinforcement

phase and matrix is therefore essential to develop a new type of high-performance nanocomposite.

■ AUTHOR INFORMATION

Corresponding Author

*Fax: 82-42-350-3910. Tel: 82-42-350-3917. E-mail: h_lee@kaist.ac.kr.

Present Addresses

[†]Center for Advanced Separation Technologies, Virginia Tech, Blacksburg, Virginia 24061, and National Energy Technology Laboratory, Morgantown, West Virginia 26507

Author Contributions

[†]These authors contributed equally to this work.

■ ACKNOWLEDGMENT

This research was supported by a National Research Foundation of Korea (NRF) grants (Leading Research Support Program, 2010-0029176; WCU program, 31-2008-000-10055-0) funded by the Ministry of Education and Science & Technology (MEST). We are grateful to KBSI (Korea Basic Science Institute) for assistance with the TEM experiment.

■ REFERENCES

- (1) Ajayan, P. M.; Schadler, L. S.; Braun, P. B. *Nanocomposite Science and Technology*; Wiley VCH: Weinheim, Germany, 2003.
- (2) Kojima, Y.; Usuki, A.; Kawasumi, M.; Okada, A.; Fukushima, Y.; Kurauchi, T.; Kamigaito, O. *J. Mater. Res.* **1993**, *8*, 1185–1189.
- (3) (a) Sariciftci, N. S.; Smilowitz, L.; Heeger, A. J.; Wudl, F. *Science* **1992**, *258*, 1474–1476. (b) Stankovich, S.; Dikin, D. A.; Dommett, G. H. B.; Kohlhaas, K. M.; Zimney, E. J.; Stach, E. A.; Piner, R. D.; Nguyen, S. T.; Ruoff, R. S. *Nature* **2006**, *442*, 282–286.
- (4) (a) Ziolo, R.; Giannelis, E.; Weinstein, B.; O'horo, M.; Ganguly, B.; Mehrotra, V.; Russell, M.; Huffman, D. *Science* **1992**, *257*, 219–223. (b) Hu, J.; Li, L.-s.; Yang, W.; Manna, L.; Wang, L.-w.; Alivisatos, A. P. *Science* **2001**, *292*, 2060–2063. (c) Sanchez, C.; Lebeau, B.; Chaput, F.; Boilot, J.-P. *Adv. Mater.* **2003**, *15*, 1969–1994.
- (5) Alexandre, M.; Dubois, P. *Mater. Sci. Eng. R* **2000**, *28*, 1–63.
- (6) Bashyam, R.; Zelenay, P. *Nature* **2006**, *443*, 63–66.
- (7) Ray, S. S.; Okamoto, M. *Prog. Polym. Sci.* **2003**, *28*, 1539–1641.
- (8) Mark, J. E. *Polym. Eng. Sci.* **1996**, *36*, 2905–2920.
- (9) Capadona, J. R.; Berg, O. V. D.; Capadona, L. A.; Schroeter, M.; Rowan, S. J.; Tyler, D. J.; Weder, C. *Nat. Nanotechnol.* **2007**, *2*, 765–769.
- (10) Wang, X.; Zhong, J.; Wang, Y.; Yu, M. *Carbon* **2006**, *44*, 1560–1564.
- (11) Finlay, K.; Gawryla, M. D.; Schiraldi, D. A. *Ind. End. Chem. Res.* **2008**, *47*, 615–619.
- (12) Atwood, J. L.; Davies, J. E. D.; MacNicol, D. D. *Inclusion Compounds*; Academic Press: London, 1984.
- (13) Dyadin, Yu. A.; Udashin, K. A. *J. Struct. Chem.* **1987**, *28*, 394–432.
- (14) Ratcliffe, C. I.; Garg, S. K.; Davidson, D. W. *J. Inclusion Phenom. Mol. Recognit. Chem.* **1990**, *8*, 159–175.
- (15) (a) Opallo, M.; Tymosiak-Zielinska, A.; Borkowska, Z. *Solid State Ionics* **1997**, *97*, 247–252. (b) Prokopowicz, A.; Opallo, M. *Solid State Ionics* **2001**, *145*, 407–413. (c) Borkowska, Z.; Opallo, M.; Tymosiak-Zielinska, A.; Zoltowski, P. *Colloids Surf., A* **1998**, *134*, 67–73. (d) Cha, J.-H.; Shin, K.; Choi, S.; Lee, H. *J. Phys. Chem. C* **2008**, *112*, 10573–10578. (e) Choi, S.; Shin, K.; Lee, H. *J. Phys. Chem. B* **2007**, *111*, 10224–12030. (f) Cha, J.-H.; Lee, W.; Lee, H. *J. Mater. Chem.* **2009**, *19*, 6542–6547.
- (16) (a) Borkowska, Z.; Tymosiak, A.; Opallo, M. *J. Electroanal. Chem.* **1996**, *406*, 109–117. (b) Kuriyama, N.; Sakai, T.; Miyamura, H.; Kato, A.; Ishikawa, H. *J. Electrochem. Soc.* **1990**, *137*, 355–356. (c) Kuriyama, N.; Sakai, T.; Miyamura, H.; Kato, A.; Ishikawa, H. *Solid State Ionics* **1990**, *40/41*, 906–909. (d) Sun, J.; MacFarlane, D. R.; Forsyth, M. *Electrochim. Acta* **2003**, *48*, 1971–1976.
- (17) Cha, J.-H.; Lee, W.; Lee, H. *Angew. Chem., Int. Ed.* **2009**, *48*, 8687–8690.
- (18) (a) Kermani, M.; Farzaneh, M.; Gagnon, R. *Cold Reg. Sci. Technol.* **2007**, *49*, 195–205. (b) Schulson, E. M. *Acta Metall. Mater.* **1990**, *38*, 1963–1976.
- (19) Bragg's law is represented by the following equation: $n\lambda = 2d \sin \theta$, where n , λ , d , and θ are an integer, wavelength, lattice spacing, and the angle between the incident and crystal plane, respectively.
- (20) Tjong, S. C. *Mater. Sci. Eng. R* **2006**, *53*, 73–197.
- (21) Raka, L.; Bogoeva-Gaceva, G.; Lu, K.; Loos, J. *Polymer* **2009**, *50*, 3739–3746.
- (22) (a) Cappadonna, M.; Erning, J. W.; Niaki, S. M. S.; Stimming, U. *Solid State Ionics* **1995**, *77*, 65–69. (b) Zaretskii, A. V.; Petrenko, V. F.; Trukhanov, A. V.; Chesnakov, V. A. *Solid State Ionics* **1989**, *36*, 225–226.